http://eprints.gla.ac.uk/149298/

1

2

3

4

5

Neon diffusion kinetics and implications for cosmogenic neon

paleothermometry in feldspars

Marissa M. Tremblay[1,2,*], David L. Shuster[1,2], Greg Balco[2], and William S. Cassata[3]

1. Department of Earth and Planetary Science, University of California, Berkeley, 307 McCone Hall #4767, Berkeley, CA 94720-4767, USA
2. Berkeley Geochronology Center, 2455 Ridge Road, Berkeley, CA 94709, USA
3. Chemical Sciences Division, Lawrence Livermore National Laboratory, 7000 East Avenue (L-231), Livermore, CA 94550, USA

[*]Corresponding author.

Email addresses: mtremblay@berkeley.edu (M.M. Tremblay), dshuster@berkeley.edu (D.L. Shuster), balcs@bgc.org (G. Balco), cassata2@llnl.gov.
Phone number: 603-203-4976 (M.M. Tremblay)

24

25

26

27

28

29

30   **Abstract**

31   Observations of cosmogenic neon concentrations in feldspars can potentially be used to constrain

32   the surface exposure duration or surface temperature history of geologic samples. The

33   applicability of cosmogenic neon to either application depends on the temperature-dependent

34   diffusivity of neon isotopes. In this work, we investigate the kinetics of neon diffusion in

35   feldspars of different compositions and geologic origins through stepwise degassing experiments

36   on single, proton-irradiated crystals. To understand the potential causes of complex diffusion

37   behavior that is sometimes manifest as nonlinearity in Arrhenius plots, we compare our results to

38   argon stepwise degassing experiments previously conducted on the same feldspars. Many of the

39   feldspars we studied exhibit linear Arrhenius behavior for neon whereas argon degassing from

40   the same feldspars did not. This suggests that nonlinear behavior in argon experiments is an

41   artifact of structural changes during laboratory heating. However, other feldspars that we

42   examined exhibit nonlinear Arrhenius behavior for neon diffusion at temperatures far below any

43   known structural changes, which suggests that some preexisting material property is responsible

44   for the complex behavior. In general, neon diffusion kinetics vary widely across the different

45   feldspars studied, with estimated activation energies (E_a) ranging from 83.3 to 110.7 kJ/mol and

46   apparent pre-exponential factors (D_0) spanning three orders of magnitude from 2.4 x 10^{-3} to 8.9 x

47   10^{-1} cm^{2}s^{-1}. As a consequence of this variability, the ability to reconstruct temperatures or

48   exposure durations from cosmogenic neon abundances will depend on both the specific feldspar

49   and the surface temperature conditions at the geologic site of interest.

50

51   **1. Introduction**

52   In noble gas thermochronometry, the thermal histories of geologic materials are inferred from the

53   concurrent production and thermally-activated diffusion of noble gases. These thermal histories

54   can be used to understand geologic processes occurring over a vast range of temperatures and

55   timescales, from erosion-driven exhumation of rocks over millions of years (e.g., Herman et al.,

56   2013, and references therein) to near instantaneous high-temperature impact events (e.g., Min et

57   al., 2004; Cassata et al., 2010; Jourdan et al., 2011). Feldspar minerals are frequently utilized for

58   noble gas thermochronometry because they are abundant in silicic rocks and have compositions

59   that permit high noble gas production rates from both radioactive decay (radiogenic noble gases)

60   and *in situ* nuclear interactions with secondary cosmic-ray particles (cosmogenic noble gases).

61   Since its development nearly half a century ago, feldspar ^{40}Ar/^{39}Ar thermochronometry, which

62   utilizes the production and diffusion of radiogenic ^{40}Ar, has been extensively used to study

63   crustal and surface processes both on Earth (e.g., Richter et al., 1991; Hodges et al., 2005) and

64   other planetary bodies (e.g., Turner, 1971; Shuster et al., 2010). More recently, cosmogenic

65   argon in feldspars has been used to reconstruct planetary surface temperatures (e.g., Shuster and

66   Cassata, 2015). Cosmogenic neon in feldspars can, in theory, also be used for surface

67   temperature thermochronometry (Tremblay et al., 2014a; Garrick-Bethell et al., 2017). If neon is

68   quantitatively retained in feldspars at planetary surface temperatures, cosmogenic neon

69   measurements can also be used to determine surface exposure durations (e.g., Kober et al.,

70   2005).

71

72   The production and diffusion systematics of a particular noble gas–mineral pair must be known

73   for thermochronometric or geochronologic applications. Here, we focus on empirical

74   quantification of neon diffusion kinetics in feldspars, with the goal of examining whether

75   cosmogenic neon can be used for surface paleothermometry (Tremblay et al., 2014a). The only

76   existing constraints on neon diffusion in feldspars were reported by Gourbet et al. (2012), who

77   examined the diffusion kinetics of neutron-induced [22]Ne in three alkali feldspars through

78   stepwise degassing experiments. Orthoclase and Ca-rich anorthoclase exhibited relatively simple

79   neon diffusion behavior expressed as a linear relationship between the logarithm of diffusivity

80   and inverse temperature (although the linearity of the orthoclase experiment has been questioned

81   (Lovera et al., 2015)), while Fish Canyon Tuff sanidine did not. The range in Arrhenius diffusion

82   parameters (activation energy, E_a, and pre-exponential factor, D_0) calculated by Gourbet et al.

83   (2012) suggest that neon can be quantitatively retained at Earth surface temperatures over

84   millions of years, in the case of the orthoclase studied, or diffusively lost on thousand year

85   timescales, in the case of anorthoclase and sanidine.

86

87   Several questions remain from these initial experiments reported by Gourbet et al. (2012) that we

88   aim to address. First, what is the kinetics of neon diffusion in plagioclase feldspars? Gourbet et

89   al. (2012) studied three alkali feldspars; no experimental work has quantified the kinetics of neon

90   diffusion in plagioclases. To fill this gap, we present results from stepwise degassing

91   experiments on three plagioclase feldspars. We also discuss results from a stepwise degassing

92   experiment on an endmember plagioclase feldspar from lunar sample 76535 (Garrick-Bethell et

93   al., 2017).

94

95   Second, how do the kinetics and behaviors of neon and argon diffusion compare? In contrast to

96   neon, there is a vast literature exploring the kinetics of argon diffusion in feldspars. Some of the

97   earliest studies examining argon in geologic materials (e.g., Reynolds, 1957; Fechtig et al., 1960;

98   Evernden et al., 1960; Gerling et al., 1963) found evidence for complex diffusion behavior in

4

99   feldspars, which has been observed numerous times since (e.g. Lovera et al., 1997, and

100   references therein; Berger and York, 1981; Harrison and McDougall, 1982; Cassata and Renne,

101   2013). The origin and significance of complex argon diffusion behavior, which is observed as

102   both nonlinear Arrhenius arrays and age spectra with multiple plateaus, has been discussed at

103   length. Multiple diffusion domain (MDD) theory (Lovera and Richter, 1989; Lovera et al., 1991;

104   Harrison et al., 1991) posits that complex diffusion behavior results from argon diffusing from

105   multiple, non-interacting subgrain domains of different sizes that are stable both during the

106   geologic history and laboratory heating of a feldspar. Others have suggested that complex argon

107   diffusion behavior may also arise due to structural modifications, microtextural development,

108   fluid alteration, or some combination therein (e.g., Villa, 2006; Parsons et al., 1999; Lovera et

109   al., 2002; McLaren et al., 2007; Villa and Hanchar, 2013; Cassata and Renne, 2013). In these

110   cases, the timing of various mineralogical changes with respect to the thermal history of a

111   feldspar matter greatly to the interpretation of complex argon diffusion behavior.

112

113   For planetary surface paleothermometry using cosmogenic neon, any subgrain alteration during

114   the geologic history of a feldspar will have occurred at higher temperatures than those of interest,

115   but will likely still affect the kinetics of neon diffusion at low temperature. It is thus important to

116   distinguish complex neon behavior due to any existing crystallochemical heterogeneities from

117   that resulting from potential structural changes during laboratory heating. In previous work on

118   noble gas diffusion in quartz (Tremblay et al., 2014b), we made this distinguishment by

119   examining diffusion of both helium and neon in the same aliquots. If structural alteration during

120   laboratory heating changes diffusion kinetics, we would expect deviations from a linear

121   Arrhenius array to occur at a common temperature for both noble gases. On the other hand, if

122   some stable subgrain property is responsible for complex diffusion behavior, then we anticipate

123   the temperature at which deviation from Arrhenius linearity occurs to differ for different noble

124   gases.

125

126   In a similar manner, in this work we present neon stepwise degassing experiments on a subset of

127   the feldspars for which Cassata and Renne (2013) conducted argon stepwise degassing

128   experiments. Cassata and Renne (2013) argued that a combination of temperature-dependent

129   structural transitions and the presence of multiple diffusion domains caused deviations from

130   linear Arrhenius behavior in their experiments. Here, we designed our experiments such that the

131   majority of the neon present was released at temperatures lower than those used by Cassata and

132   Renne (2013) to characterize argon diffusion. As a result, all deviations from linear Arrhenius

133   behavior interpreted by Cassata and Renne (2013) to be a result of structural transitions should

134   be absent from our neon experiments, if their interpretation is correct. We also examined

135   feldspars that exhibit linear Arrhenius behavior for argon diffusion to determine whether simple

136   diffusion behavior is also observed for neon. If simple diffusion behavior is observed for both

137   noble gases in a particular feldspar, it suggests that there is a single diffusion domain with a

138   single diffusion lengthscale, which may equal the physical grain size of the aliquots analyzed. In

139   these cases, our experimental results and those of Cassata and Renne (2013) can be compared

140   with theoretical calculations of argon and neon diffusivities.

141

142   In addition to addressing the questions outlined above, we use our experimentally-determined

143   diffusion kinetics to model the sensitivity of cosmogenic neon diffusion to temperature and

144   exposure duration amongst different feldspars. We use the modeled sensitivities to evaluate the

145 potential for using cosmogenic neon in feldspar to constrain past planetary surface temperatures.

146

147 **2. Methods**

148 We conducted neon stepwise degassing experiments on a suite of feldspar that span the full

149 range of feldspar compositions from orthoclase to anorthite. Brief sample descriptions including

150 compositions are provided in Table 1; for more detailed information, see Cassata and Renne

151 (2013) and references therein. Samples were irradiated with a 220 MeV proton beam for 5 hours

152 at the Francis H. Burr Proton Therapy Center at the Massachusetts General Hospital. Numerous

153 grains from a given sample were packed together into an Sn foil in order to balance ejection of

154 proton-induced Ne with implantation (e.g., Shuster et al., 2004). These Sn foils were packaged

155 into HDPE capsules (9.4 mm in diameter, 3.0 in mm height), which were stacked into quartz

156 tubes to form a ~500 mm long cylindrical target; the approximate range of 220 MeV protons in

157 HDPE is 300 mm. A 100 μm thick Pb foil in front of the target stack, in conjunction with the

158 target stack itself, defocuses and scatters the proton beam intensity in attempt to evenly distribute

159 the cross-section flux (Shuster et al., 2004, Shuster and Farley, 2005a). The target was flipped

160 halfway through the irradiation to ensure Ne production in both ends of the target stack despite

161 proton energy dissipation; the feldspars examined here were located within 150 mm of either end

162 of the target stack. Sample temperatures do not exceed 45 ˚C during irradiation (Shuster and

163 Farely, 2005b). Proton irradiation of the feldspars examined here took place in April 2013 with a

164 total proton fluence of ~8.5×10^{15} p/cm^2, which was measured during irradiation by a thin foil

165 transmission ionization chamber in front of the beam aperture.

166

167 This irradiation design should lead to spatially uniform Ne production for crystal fragments <

168   500 µm in radius (Shuster and Farley, 2005a) if the crystal fragments are compositionally

169   uniform. With the exception of Fish Canyon sanidine and Grass Valley anorthite, the feldspars

170   studied here are compositionally homogeneous with respect to these elements (Cassata and

171   Renne, 2013) and we therefore expect proton-induced Ne to be spatially uniform. The production

172   of uniform, high concentrations of neon isotopes from proton irradiation allows us to conduct

173   stepwise degassing experiments on single feldspar crystals (Shuster et al., 2004; Shuster and

174   Farley, 2005b; Tremblay et al., 2014b). Implications for compositional zonation of Fish Canyon

175   sanidine and Grass Valley anorthite are detailed in the discussion.

176

177   The effects of lattice damage from proton irradiation on noble gas diffusion in feldspars has not

178   been explicitly investigated. Previous work empirically demonstrates that lattice damage

179   generated during proton irradiation with the magnitude of fluence and energy used here does not

180   significantly modify noble gas diffusion kinetics in other mineral phases (Shuster et al., 2004;

181   Shuster and Farley, 2005b; Tremblay et al., 2014). Although neutron irradiation, which typically

182   has 2–3 orders of magnitude higher fluence than proton irradiation, has been shown to influence

183   noble gas diffusion in apatite (Shuster and Farley, 2009), several studies have demonstrated that

184   damage generated during neutron irradiation minimally affects argon diffusion kinetics (Foland

185   and Xu, 1990; Lovera et al., 1993; Cassata and Renne, 2013). Given this set of observations, we

186   therefore assume that damage produced during proton irradiation does not significantly modify

187   neon diffusion kinetics in feldspars, although this assumption should be tested with replicate

188   experiments on aliquots irradiated with different proton fluences and energies.

189

190   Proton irradiated feldspars were inspected by binocular microscopy to select individual crystals

191   lacking penetrative fractures and visible inclusions. Selected crystals were photographed to

192   estimate crystal dimensions (Fig. S1) and then placed under vacuum inside Pt-Ir alloy packets

193   affixed to K-type thermocouples. Packets were heated with either a 30 or 150 W diode laser in a

194   feedback control loop with the thermocouple via a PID temperature controller, enabling us to

195   maintain a setpoint temperature to within 2 °C. Samples were heated in fifty or more consecutive

196   heating steps to temperatures between 100 and 1200 °C. Each heating schedule contained at least

197   two retrograde heating cycles, and individual heating steps lasted between 0.5 and 4 hours. All

198   measurements were made on an MAP 215-50 sector field mass spectrometer in the Noble Gas

199   Thermochronometry Lab of the Berkeley Geochronology Center; gas purification and mass

200   spectrometric measurement techniques are detailed in Tremblay et al. (2014b). For ^{21}Ne, we

201   made no isobaric interference corrections; the MAP 215-50 cannot resolve ^{20}Ne^{1}H from ^{21}Ne,

202   and we assume corrections due to this isobaric interference are negligible. ^{21}Ne background

203   corrections were made by subtracting the average of six or more room temperature procedural

204   blanks measured over the course of each experiment from measurement time-zero intercepts; the

205   average correction for ^{21}Ne across all experiments was 0.06 x 10^6 atoms. ^{20}Ne and ^{22}Ne have

206   isobaric interferences from ^{40}Ar^{++} and ^{44}CO$_2^{++}$, respectively, which the MAP 215-50 sector field

207   mass spectrometer used for these experiments also cannot resolve. Although these interferences

208   can be corrected for by introducing an ^{39}Ar spike during neon measurements and observing a

209   linear relationship between the Ar^{++}/Ar$^+$ and CO$_2^{++}$/CO^{2+} ratios (Balco and Shuster, 2009), we

210   did not use the spike procedure during these experiments. Instead, we assumed that all of the

211   ^{22}Ne signal observed during room-temperature procedural blanks was entirely from ^{44}CO$_2^{++}$ and

212   used the average blank 44/22 ratio and measured ^{44}CO$_2^+$ signals to correct measured ^{22}Ne signals

213   during heating steps. ^{20}Ne was not measured. Experiments were terminated when three or more

214   consecutive heating steps yielded ^{21}Ne and ^{22}Ne time-zero intercepts at or below background

215   level. We determined total neon amounts by comparison with the time-zero intercepts of a

216   manometrically-calibrated air standard. Measurement of different calibrated pipette volumes of

217   the air standard demonstrated that ^{21}Ne sensitivity was constant over the pressure range of the

218   analyses in a given experiment. Blank corrected ^{21}Ne and ^{22}Ne abundances for each heating step

219   are reported in Table S1. The magnitude of the isobaric interference correction on ^{22}Ne signals

220   for individual heating steps varies between 5 and 100%, with an average correction of ~50%.

221   These generally large-magnitude corrections propagate into very large ^{22}Ne uncertainties;

222   therefore we do not use the ^{22}Ne data further. The concentrations of ^{21}Ne and ^{22}Ne present in the

223   individual feldspar crystals analyzed (> 10^{12} atoms/g) are orders of magnitude greater than any

224   likely combination of atmospheric, cosmogenic, and nucleogenic neon components present prior

225   to proton irradiation, which for terrestrial samples are typically on the order of 10^{6}–10^{8} atoms/g

226   (e.g., Gourbet et al., 2012; Kober et al., 2005). We therefore assume that contributions from

227   these components are negligible in comparison to the uniformly distributed, proton-induced

228   neon, and that variations in the ^{21}Ne/^{22}Ne ratio between different heating steps reflect the very

229   uncertain isobaric interference correction made for ^{22}Ne.

230

231   We used the equations of Fechtig and Kalbitzer (1966) to calculate lengthscale-normalized

232   diffusivities (D/a^2) from the fraction of ^{21}Ne measured and duration of each heating step for each

233   stepwise degassing experiment. By using these equations, we make several assumptions. First,

234   we assume that Ne diffusion is both Fickian and isotropic (Crank, 1975). Ar stepwise degassing

235   experiments on cleavage flakes with different lattice orientations indicate isotropic diffusion in

236   feldspars at the temperatures over which we conduct neon step degassing experiments (Cassata

237   and Renne, 2013). Second, we assume that the initial distribution of the diffusant is spatially

238   uniform; proton irradiation should generate Ne uniformly, as discussed above. Third, we assume

239   that each feldspar crystal has a spherical, fixed geometry. We approximate the spherically

240   equivalent radius of the samples used in our experiments as the radius of a sphere whose surface

241   area to volume ratio equals that of the crystal analyzed. Previous work demonstrates that this

242   assumption is valid for materials with moderate aspect ratios, even for crystals with realistic

243   shapes or irregular geometries (Meesters and Dunai, 2002; Gautheron and Tassan-Got, 2010;

244   Huber et al., 2011).

245

246   We first estimated the surface to volume ratio of the crystals from optical microscopy

247   measurements. Since feldspars do not have distinctive crystal habits and frequently bear surface

248   irregularities such as cleavage steps, we had to make simplifying assumptions about the crystal

249   geometries to make these estimates. To overcome this limitation, we obtained accurate surface

250   area to volume ratio and size determinations of the feldspar crystals by X-ray computed

251   tomography. X-ray computed tomography (CT) allows for three-dimensional, nondestructive

252   characterization of geologic samples based on the variable attenuation of X-rays as they travel

253   through different materials (Ketcham and Carlson, 2001). After the stepwise degassing

254   experiments, we extracted each crystal from its packet to look for evidence of fracturing. Intact

255   fragments were mounted on double sided tape and scanned with 3.15 μm resolution on the

256   Xradia MicroXCT scanner at the University of Texas at Austin High-Resolution X-ray CT

257   Facility. Using the software Blob3D (Ketcham, 2005), feldspar crystals were segmented from

258   mounting material using a grayscale threshold and separated into individual crystal volumes. We

259   extracted numerous statistics about these volumes, including surface area, volume, aspect ratio,

260   and maximum and minimum axis lengths, and calculated spherically equivalent radii of the

261   crystals for comparison with our first estimates (Table S2).

262

263   **3. Results**

264   Results of the neon stepwise degassing experiments are reported in Table S1 and plotted in Figs.

265   1A–6A, where the natural logarithm of calculated diffusivities ($ln(D/a^2)$, where D is diffusivity

266   and a is the diffusive lengthscale) is shown as a function of inverse temperature. Figs. 1A–6A

267   also show the results from argon stepwise degassing experiments on different grains of the same

268   feldspars reported by Cassata and Renne (2013). Additionally, in Fig. 7 we compare the result of

269   a neon stepwise degassing experiment on a neutron-irradiated crystal of anorthite from lunar

270   troctolite 76535 (Garrick-Bethell et al., 2017) to an [37]Ar stepwise degassing experiment on

271   76535 anorthite reported by Cassata and Renne (2013). For both neon and argon datasets, we use

272   the Monte Carlo approach described by Tremblay et al. (2014b) to propagate uncertainties in gas

273   release fraction into calculated diffusivities. If the temperature dependence of noble gas diffusion

274   is Arrhenian and the feldspar analyzed is characterized by a single diffusion domain, then we

275   expect to observe a linear correlation in this plotting space. In many cases we observe significant

276   deviations from linearity; however, for all stepwise degassing experiments at least a subset of the

277   data collected comprises a linear array. We fit least squares regressions to these subsets in Figs.

278   1A–7A, with the goal of including as many temperature steps as possible in the regression while

279   minimizing the residuals between the regression and the data. We used these regressions and the

280   Monte-Carlo derived uncertainties in D/a^2 to estimate the activation energy (E_a) and diffusion

281   coefficient (D_0/a^2) from the slope and intercept of the linear regression, respectively, assuming

282   an Arrhenius dependence of diffusivity on temperature:

283
$$\frac{D}{a^2} = \frac{D_0}{a^2} exp\left(\frac{-E_a}{RT}\right)$$

284   where R is the gas constant and T is absolute temperature. These calculated diffusion parameters

285   are reported in Table 2. While the significance of these calculated diffusion parameters is in

286   some cases uncertain, as will be discussed below, fitting these regressions allows us to compare

287   the temperatures and gas fractions over which linear Arrhenius behavior is observed. These

288   comparisons are shown in Figs. 1B–7B and 1C–7C as residuals, which we define as the

289   difference between the calculated diffusivity from a given heating step and the expected

290   diffusivity from the linear regression at the same temperature.

291

292   The two neon stepwise degassing experiments we conducted on Fish Canyon sanidine exhibited

293   single linear Arrhenius arrays over the duration of the experiment, which was also observed in

294   replicate argon stepwise degassing experiments (Fig. 1). Deviation from linearity occurs at the

295   end of neon experiment A; however, this deviation comprises less than 7% of the cumulative

296   ^{21}Ne released (Fig. 1C), and the remaining steps do not form any clear additional linear arrays

297   (Fig. 1A). Interestingly, our stepwise degassing experiments using proton-induced ^{21}Ne disagree

298   significantly with the experiment using neutron-induced ^{22}Ne reported by Gourbet et al. (2012),

299   which showed complex neon diffusion behavior (Fig.1A). Neon and argon stepwise degassing

300   experiments on Gulf of Salerno sanidine likewise exhibit simple, linear Arrhenius behavior (Fig.

301   2). Although several of the high-temperature steps in the neon stepwise degassing experiment

302   deviate from a linear Arrhenius array (Fig. 2B), these steps constitute less than 10% of the

303   cumulative ^{21}Ne released (Fig. 2C) and do not form any clear additional linear arrays (Fig. 2A).

304

305   Feldspars other than sanidine exhibit disparate neon and argon Arrhenius behavior. The neon

306   experiment on Benson Mines orthoclase shows a clear downward deviation from linear

307   Arrhenius behavior at ~70% of the cumulative ^{21}Ne release fraction (Figs. 3A and 3C). A second

308   linear Arrhenius array, which includes a retrograde heating cycle, is observed at higher ^{21}Ne

309   release fractions (Fig. 3A). For comparison, we show the results of an ^{39}Ar stepwise degassing

310   experiment reported by Cassata and Renne (2013) on an equant crystal of Benson Mines

311   orthoclase with an estimated spherical radius equal to that in the neon experiment. The ^{39}Ar

312   experiment appears to comprise a single linear Arrhenius array (Fig. 3A). There is a slight

313   downward deviation in diffusivity between 50 and 70% of the cumulative ^{39}Ar released as well

314   (Fig. 3C). However, the steps following this downward deviation occur at temperatures

315   exceeding 1100 °C (Fig. 3B), at which point the crystal used in the ^{39}Ar experiment is melting

316   (Schairer, 1950; Parsons, 2010). The two labradorite samples studied from Surtsey, Iceland and

317   Plush, Oregon, both exhibit upward deviations from linear Arrhenius behavior in ^{37}Ar stepwise

318   degassing experiments at temperatures between 600 and 800 °C and at gas release fractions <

319   10% (Figs. 4 and 5; Cassata and Renne, 2013). Essentially all of the ^{21}Ne in our stepwise

320   degassing experiment on Surtsey labradorite was released during steps below 600 °C (Fig. 4C)

321   and comprises a single linear Arrhenius array (Fig. 4A). The ^{21}Ne step degassing experiment on

322   Plush labradorite, on the other hand, shows a significant downward deviation from an initial

323   linear Arrhenius array at 350 °C and 25% of the cumulative ^{21}Ne released (Fig. 5). Lastly, we

324   compare neon and argon degassing experiments on two samples of anorthite, the calcium

325   endmember of plagioclase feldspar. In Grass Valley anorthite, neon and argon both show

326   downward deviations from linear Arrhenius behavior, but at different temperatures and gas

327   release fractions (Fig. 6). Anorthite from lunar sample 76535 shows linear Arrhenius behavior

328   for 97% of the ^{21}Ne measured but downward deviation from linear behavior at 30% of the

329   cumulative ^{37}Ar and 1000 °C.

330

331   For the subset of each dataset comprising a linear Arrhenius array, we find that ^{21}Ne activation

332   energies range from 83.3 to 110.7 kJ/mol and apparent pre-exponential factors (D_0) range from

333   2.4 x 10^{-3} to 1.99 x 10^2 cm^{2}s^{-1}. These diffusion parameters are within the range of those

334   calculated by Gourbet et al. (2012) for three alkali feldspars. Activation energies and apparent

335   pre-exponential factors for ^{21}Ne diffusion in plagioclase feldspars are generally greater than

336   those in alkali feldspars, although a larger number of neon stepwise degassing experiments are

337   necessary to determine if this trend is systematic. Roughly the opposite trend was observed for

338   the activation energy of argon diffusion as a function of composition (Cassata and Renne, 2013).

339

340   **4. Discussion**

341   While argon diffusion in feldspars has been studied at length over several decades, this is only

342   the second work to examine neon diffusion in feldspars and the first work to study neon diffusion

343   in plagioclase feldspars. As such, these neon stepwise degassing experiments provide insight into

344   the potential noble gas diffusion mechanisms in feldspars. Below we discuss evidence for both

345   structural modifications and multiple diffusive lengthscales affecting noble gas diffusion in

346   feldspars. For feldspars that exhibit complex neon diffusion behavior, we construct multiple

347   diffusion domain (MDD) models. We use the diffusion parameters from these MDD models as

348   well as the diffusion parameters determined for feldspars exhibiting simple Arrhenius behavior

349   to explore the temperatures and exposure durations over which cosmogenic neon-in-feldspar

350   paleothermometry can be applied to study past surface temperatures.

351

4.1 Comparison of neon and argon diffusion

4.1.1 Neon and argon diffusion in alkali feldspars

Of the samples we examined, Fish Canyon and Gulf of Salerno sanidine exhibited the simplest Arrhenius behavior for argon diffusion (Figs. 1 and 2; Cassata and Renne, 2013). A single linear Arrhenius array characterizing all of the ^{39}Ar released during these experiments is consistent with a single diffusion lengthscale, which we assume is equal the grain size analyzed (in which case a ≈ 213, 332, and 407 μm for Fish Canyon sanidine 1, Fish Canyon sanidine 2, and Gulf of Salerno sanidine respectively, which we estimated from the total amount of ^{39}Ar, the duration of the neutron irradiation, and the stoichiometry of each feldspar). Cassata and Renne (2013) also attribute simple behavior to the fact that sanidine has monoclinic crystal symmetry at room temperature and does not undergo a displacive transition during heating. Consequently, thermal expansion proceeds linearly in all three unit cell directions (Brown et al., 1984; Hovis et al., 1999). Our proton-induced ^{21}Ne stepwise degassing experiments on Fish Canyon and Gulf of Salerno sanidine also exhibit simple diffusion behavior, with ≥ 90% of the ^{21}Ne degassed plotting on a single linear Arrhenius array and no additional arrays formed from the few high temperatures steps that deviate. The neutron-induced ^{22}Ne stepwise degassing experiment on Fish Canyon sanidine reported by Gourbet et al. (2012) seemingly conflicts with our observation of simple neon diffusion behavior (Fig. 1A). One possibility is that the crystal fragment used in the neutron-irradiated experiment was fractured before or during the stepwise degassing experiment. Another possibility is that heating to > 250 °C during neutron irradiation caused some diffusive loss of neon. This latter possibility seems likely given the diffusion kinetics we determined for Fish Canyon sanidine; however, we would expect the initial neon data from the neutron-irradiated experiment to plot below the linear Arrhenius array in the proton-irradiated

375   experiment if this were the case. Gourbet et al. (2012) suggest that production of ^{22}Ne from the

376   spallation reaction ^{23}Na(n,np)^{22}Ne during neutron irradiation may have been spatially variable

377   due to core-to-rim zonation of Na in Fish Canyon sanidine (Bachmann et al., 2002). Spatially

378   variable ^{22}Ne production violates the assumption of a uniform initial ^{22}Ne distribution and could

379   lead to curved Arrhenius arrays. However, if spatially variable production of ^{22}Ne from ^{23}Na was

380   the cause of nonlinear behavior, we would expect to observe nonlinear behavior in the argon

381   experiments as well, given that ^{39}Ar is produced from ^{39}K and K is also zoned in Fish Canyon

382   sanidine (Bachmann et al., 2002). Curvature in the proton-irradiated neon experiments might

383   also be expected if this were the case, although spatially variable production from ^{23}Na would be

384   buffered by reactions on Al and Si with similar cross sections (Koning et al., 2015). Given these

385   numerous potential complications with the Fish Canyon sanidine experiment reported by

386   Gourbet et al. (2012), we suggest that our stepwise degassing experiments using proton-

387   irradiated Fish Canyon sanidine more accurately characterize neon diffusion in that sample. Our

388   ^{21}Ne results, when paired with the ^{39}Ar stepwise degassing experiments, strongly support the

389   case for these sanidine samples having a single diffusion domain with a single diffusion

390   lengthscale, which we assume is defined by the physical grain size. Additionally, the diffusion

391   parameters (E_a and D_0) for Fish Canyon and Gulf of Salerno sanidine are in good agreement with

392   one another for the respective noble gases examined. The diffusion parameters reported in Table

393   2 for Fish Canyon and Gulf of Salerno sanidine can therefore be straightforwardly compared to

394   theoretical calculations (e.g., density functional theory or molecular dynamics simulations) of

395   interstitial neon and argon diffusion through the monoclinic sanidine crystal structure.

396

397   The Arrhenius behavior of ^{21}Ne diffusion in Benson Mines orthoclase is somewhat surprising, as

398 monoclinic orthoclase is also expected to undergo linear thermal expansion. Cassata and Renne

399 conducted five argon stepwise degassing experiments on Benson Mines orthoclase, one on an

400 equant fragment (Fig. 3) and four on sheet-like cleavage fragments (Fig. S2). All five

401 experiments exhibit deviations from a linear Arrhenius array at high temperatures and ^{39}Ar

402 release fractions; however, in all experiments these deviations occur near the melting point of

403 orthoclase (Schairer, 1950; Parsons, 2010), making it difficult to assess its origin. The ^{21}Ne

404 stepwise degassing experiment on Benson Mines orthoclase, on the other hand, shows a clear

405 downward deviation from linear Arrhenius behavior beginning at 70% of the cumulative ^{21}Ne

406 released and at 500 °C, hundreds of degrees below the melting temperature of orthoclase (Fig. 3).

407 There was no visible evidence for fracturing or other alteration when we unpacked the crystal for

408 X-Ray CT analysis, indicating that no change in the physical grain size occurred before or during

409 the experiment. Additionally, a second linear Arrhenius array observed at higher temperatures

410 and gas release fractions in the ^{21}Ne experiment includes a retrograde heating cycle (Fig. 3A). If

411 nonlinear Arrhenius behavior resulted from a reversible, temperature-dependent structural

412 transformation, we would expect diffusivities in the retrograde heating to approach diffusivities

413 observed at the same temperatures in the preceding prograde heating, which was not observed.

414 These observations leave two potential explanations for the nonlinear Arrhenius behavior. It is

415 possible that the crystal of Benson Mines orthoclase we analyzed was fractured in a way that was

416 not detected by either optical microscopy or X-ray CT, in which case replicating the neon step

417 degassing experiment on a different crystal of Benson Mines orthoclase would result in different

418 Arrhenius behavior. Alternatively, these results could indicate that nonlinear Arrhenius behavior

419 of ^{21}Ne reflects a preexisting material property (sub-grain domain distribution) of Benson Mines

420 orthoclase. This latter possibility suggests that the same intrinsic property of Benson Mines

421   orthoclase ought to cause nonlinear Arrhenius behavior for argon. Deviations from linearity

422   observed in argon experiments reported by Cassata and Renne (2013) occur between 15 and 80%

423   of the Ar released, which at first appears to suggest that sub-grain features defining the diffusion

424   lengthscale vary from grain to grain. However, these deviations all occur near the melting

425   temperature of orthoclase, making the origin of these deviations ambiguous. A straightforward

426   test of this hypothesis would be to conduct another [39]Ar stepwise degassing experiment on

427   Benson Mines orthoclase with a revised heating schedule, such that all of the [39]Ar is released at

428   temperatures significantly below the orthoclase melting temperature.

429

430   *4.1.2 Neon and argon diffusion in plagioclase feldspars*

431   Our neon stepwise degassing experiments on plagioclase feldspars highlight how the effects of

432   both structural modification during laboratory heating and preexisting material properties can be

433   convoluted to result in nonlinear Arrhenius behavior. Cassata and Renne (2013) conducted a

434   number of experiments on labradorite samples, all of which exhibit upward deviations from

435   initial linear Arrhenius arrays at temperatures between 600 and 800 °C. They argue that in

436   labradorite and other Ca-rich feldspars, upward deviations are the result of an increase in the rate

437   of thermal expansion above 600 °C, which has been observed experimentally (Tribaudino et al.,

438   2010; Hovis et al., 2010). This interpretation is consistent with our neon stepwise degassing

439   experiments on Surtsey and Plush labradorite, as we observed no upward deviations from an

440   initial Arrhenius array and degas > 99% of the [21]Ne below 600 °C in both experiments (Figs. 4

441   and 5). However, in the case of Plush labradorite, we observe a downward deviation from an

442   initial linear Arrhenius array when ~25% of the [21]Ne had been released and at 350 °C (Fig. 5), a

443   temperature for which no changes in the rate of thermal expansion are expected. Like our neon

444   degassing experiment on Benson Mines orthoclase, retrograde heating steps in the Plush

445   labradorite experiment do not overlap with the initial linear Arrhenius array, confirming that this

446   behavior is not a result of a reversible structural change. If we assume that the crystal of Plush

447   labradorite was not fractured, these results instead suggest that complex neon diffusion behavior

448   reflects a preexisting material property of Plush labradorite. A very small fraction (< 10%) of the

449   total gas is released below 600 °C in argon stepwise degassing experiments; therefore the effects

450   of this preexisting material property are likely obscured by the coincident changes in rate of

451   thermal expansion. Without the observation of temperature-independent complex Arrhenius

452   behavior from the neon stepwise degassing experiment on Plush labradorite, simple down-

453   temperature extrapolation of the initial linear Arrhenius array in the argon stepwise degassing

454   experiment to geologically relevant temperatures may have seem justified. However, doing so

455   would likely result in inaccurate thermal history reconstruction. In contrast to Plush labradorite,

456   with Surtsey labradorite we observe a single linear Arrhenius array for ^{21}Ne (Fig. 4), suggesting

457   this labradorite is characterized by a single diffusion domain with a single diffusion lengthscale,

458   which may be defined by the physical grain size (a ≈ 307 μm). Furthermore, this implies that

459   nonlinear behavior for Ar diffusion, manifest as upward curvature on Arrhenius plots at ~600 °C,

460   followed by downward curvature at higher temperatures, is likely related to structural

461   modifications of the feldspar in response to heating (Cassata and Renne, 2013). Accurate

462   geologic thermal history information could therefore be inferred for Surtsey labradorite by

463   downward extrapolation of initial linear Arrhenius arrays.

464

465   Unlike the other feldspars we studied, anorthite undergoes a structural transition during neon

466   stepwise degassing experiments. Between 225 and 300 °C, anorthite transitions from a *P1* to *T*

467   triclinic crystal symmetry (Smith and Ribbe, 1969; Van Tendeloo et al., 1989). The *P1–T*

468   transition is accompanied by an increase in unit cell volume and in the rate of thermal expansion

469   (Tribaudino et al., 2010), both of which ought to decrease the energy barrier to interstitial

470   diffusion and increase noble gas diffusivities. Therefore we expect to observe upward deviations

471   from initial linear Arrhenius arrays associated with this transition in neon stepwise degassing

472   experiments but not in argon stepwise degassing experiments, as the latter take place at

473   temperatures above the *P1–T* transition. In the ^{21}Ne stepwise degassing experiment on Grass

474   Valley anorthite, we observed the opposite: downward deviation from an initial linear Arrhenius

475   array occurred at 300 °C (Fig. 6). However, we do not find this surprising given the

476   crystallochemical complexity of Grass Valley anorthite, which is characterized by two phases of

477   anorthite separated by antiphase boundaries, as well large muscovite inclusions, plagioclase

478   subgrains, and Na-rich feldspar alteration patches (McLaren and Marshall, 1974; Rainey and

479   Wenk, 1978). Thus we anticipate both the diffusion kinetics and initial distribution of neon to be

480   spatially variable in this sample. Given this heterogeneity, it is also expected that the argon and

481   neon diffusion experiments on different aliquots of Grass Valley anorthite are not reconcilable

482   with one another. A neon stepwise degassing experiment on neutron-irradiated anorthite from

483   lunar sample 76535 (Garrick-Bethell et al., 2017) exhibits linear Arrhenius behavior between

484   170 and 800 °C for essentially all of the gas released (Fig. 7). There appears to be a slight

485   upward deviation in the diffusivities at ~300 °C, which may be associated with the *P1–T*

486   transition. However, fitting a linear regression to only the data collected below 300 °C yields

487   indistinguishable diffusion parameters from those calculated using all the data. Linear Arrhenius

488   behavior at temperatures below 800 °C in the neon experiment is also consistent with the

489   downward deviation from an initial linear Arrhenius array above 800 °C in the argon experiment

490 being caused by the transition to an *I1* symmetry (Megaw et al., 1962; Foit and Peacor, 1973).

491

492 To summarize our comparison of neon and argon stepwise degassing experiments, we often see

493 different Arrhenius behavior for neon diffusion than was observed for argon diffusion in the

494 same feldspars. The origin of these differences depends on the feldspar in question. In several

495 cases, the effects of a preexisting material property of a particular feldspar and the effects of a

496 structural transformation during laboratory heating are conflated in argon stepwise degassing

497 experiments; neon stepwise degassing experiments conducted at lower temperatures make such

498 conflations apparent. It would be valuable to measure neon and argon isotopes simultaneously in

499 future stepwise degassing experiments on neutron-irradiated feldspars in order to discern

500 between such effects.

501

502 **4.2 Multiple diffusion domain (MDD) model for neon diffusion in feldspars**

503 At present, we cannot ascribe a specific intrinsic property or mechanism to nonlinear Arrhenius

504 behavior that is not associated with a temperature-dependent structural transformation.

505 Identifying the origin of this complex Arrhenius behavior in argon stepwise degassing

506 experiments is critically important, because crystallochemical changes that could potentially be

507 responsible for this behavior (e.g., strain-induced microtextural development, fluid alteration)

508 may have occurred during the portion of a sample's geologic thermal history that is relevant to

509 $^{40}Ar/^{39}Ar$ thermochronometry. For cosmogenic noble gas thermochronometry using neon in

510 feldspars, wherein production and diffusion are only happening at planetary surfaces where

511 feldspars are exposed to cosmic ray particles, we expect any major crystallochemical changes to

512 have occurred at much higher temperatures than are relevant to the system of interest. In other

513   words, all crystallochemical heterogeneities are present throughout the thermal history recorded

514   by cosmogenic neon in feldspars, with the possible exception of those generated by shock during

515   impact events. Thus although we do not have a mechanistic explanation for the nonlinear,

516   temperature-independent Arrhenius behavior observed in some neon experiments, we think this

517   complex behavior characterizes cosmogenic neon diffusivity and therefore must be accounted for

518   to accurately reconstruct temperatures using cosmogenic neon in feldspars.

519

520   In order to account for complex neon diffusion in feldspars, we modeled the results of stepwise

521   degassing experiments exhibiting complex Arrhenius behavior using multiple diffusion domain

522   (MDD) theory (Lovera and Richter, 1989; Lovera et al., 1991; Harrison et al., 1991). MDD

523   theory explains nonlinear Arrhenius behavior as the result of diffusion from multiple, non-

524   interacting subgrain domains of varying sizes. Our modeling approach is similar to that described

525   in Tremblay et al. (2014b), wherein diffusivities are calculated for the experiment heating

526   schedule using the equations outlined by Fechtig and Kalbitzer (1966) for a spherical geometry

527   and for a given diffusion domain distribution. The number of subgrain domains was allowed to

528   vary, and the models were designed to search over a large number of combinations of activation

529   energy (E_a), pre-exponential factor(D_0/a^2), and gas fraction (*f*) attributed to each domain;

530   activation energy was held in common for all domains. For a particular number of diffusion

531   domains, we determined the combination of diffusion parameters and gas fractions that best

532   agreed with the stepwise degassing experiments by calculating a misfit statistic *M*:

533
$$M = \sum_{j=1}^{n} \left| f_{p,j} - f_{m,j} \right|$$

534   where $f_{p,j}$ is the modeled cumulative [21]Ne released at heating step *j*, $f_{p,j}$ is the observed

535   cumulative ^{21}Ne released at heating step *j*, and *n* is the total number of heating steps. This misfit

536   statistic is analogous to the reduced chi-squared misfit statistic used in Tremblay et al. (2014b) in

537   that the same set of diffusion parameters minimizes both quantities. However, the cumulative

538   difference in predicted and observed gas fractions used here has more physical meaning. For

539   example, a misfit statistic of 0.15 can be thought of as not predicting 15% of the observed ^{21}Ne

540   released with our MDD model. We continued to add diffusion domains until the minimized

541   misfit statistic with *x + 1* domains was within 0.03 of the minimized misfit statistic with *x*

542   domains. In Fig. 8, we show the best fit MDD models for the neon stepwise degassing

543   experiments on Benson Mines orthoclase, Plush labradorite, and Grass Valley anorthite; best fit

544   diffusion parameters, gas fractions, and misfit statistics are reported in Table 3. By assuming that

545   this model framework can be extrapolated over time and to lower temperatures, we use the MDD

546   model fits for these feldspars in the remaining discussion to assess the sensitivity of cosmogenic

547   neon-in-feldspar paleothermometry to exposure temperature and duration.

548

549   **4.3 Implications for neon retentivity in feldspars**

550   The seven neon stepwise degassing experiments reported here, combined with the experiments

551   reported by Gourbet et al. (2012) and Tremblay and Shuster (2016), demonstrate that neon

552   diffusion kinetics and behavior vary widely amongst feldspars of different compositions and

553   geologic origins. This is perhaps not surprising, given the vast range of diffusion kinetics and

554   behavior observed in argon stepwise degassing experiments (e.g., Lovera et al., 1997; Lovera et

555   al., 2002; Cassata and Renne, 2013). Nonetheless, the variability of neon diffusion kinetics and

556   behavior has important implications for the applicability of laboratory-determined diffusion

557   kinetics to applications of cosmogenic neon paleothermometry (Tremblay et al., 2014a).

558 Specifically, these results indicate that sample-specific diffusion kinetics will be necessary to

559 quantitatively reconstruct temperatures using cosmogenic neon in feldspars.

560

561 To illustrate this point, in Fig. 9 we show how cosmogenic neon retentivity will evolve as a

562 function of exposure duration for a constant exposure temperature of 20 °C using the different

563 diffusion parameters obtained in neon stepwise degassing experiments. Retentivity refers to the

564 amount of cosmogenic neon produced during exposure to cosmic ray particles that has not

565 diffused out of the feldspar; thus a retentivity of one indicates no diffusive loss, while a

566 retentivity asymptoting to zero indicates that steady steady state between production and

567 diffusion has occurred. For feldspars exhibiting linear Arrhenius behavior, we assume that the

568 physical grain size defines the diffusion lengthscale of a single diffusion domain and scale

569 diffusivities to a common diffusion lengthscale of 500 μm; retention curves for these feldspars

570 are shown in Fig. 9A. Having normalized the diffusion lengthscale, we can see in Fig. 9A that

571 differences in diffusion parameters (E_a and D_0) amongst different feldspars results in significant

572 variability in retentivity. For example, while lunar 76535 anorthite is expected to retain all of its

573 cosmogenic neon over 10 Ma of exposure at 20 °C, Easy Chair Crater anorthoclase would retain

574 < 10% given the same exposure history. In cases where we used MDD models to infer neon

575 diffusion parameters, we do not know the diffusion lengthscale of the different domains as this

576 cannot be separated from the preexponential factor D_0 without making additional assumptions.

577 Furthermore, it is likely that the domain size distributions in feldspars exhibiting MDD-like

578 behavior would depend on macroscopic grain size in a way that we cannot quantify. We

579 therefore did the calculations in Fig. 9B using the spherically equivalent radius of each feldspar

580 crystal analyzed in the stepwise degassing experiment. Fig. 9B highlights the difference in

581 cosmogenic neon retentivities that would be expected for simple extrapolation of initial linear

582 Arrhenius arrays versus MMD model calculated diffusion parameters in feldspars exhibiting

583 complex Arrhenius behavior. For some feldspars such as Benson Mines orthoclase, the

584 differences are small until very long exposure durations are reached (> 1 Ma); for others such as

585 Grass Valley anorthite, the differences become important on much shorter timescales (> 0.01

586 Ma).

587

588 In previous theoretical calculations on the sensitivity of cosmogenic neon-in-feldspar

589 paleothermometry (Tremblay et al., 2014a), we used the diffusion kinetics for Madagascar

590 cryptoperthite reported by Gourbet et al. (2012). However as can be seen in Fig. 9, we predict

591 lower cosmogenic neon retentivity using neon diffusion kinetics from most of the feldspars we

592 examined than when using Madagascar cryptoperthite kinetics. This means that the applicability

593 of cosmogenic noble gas paleothermometry to geologic problems will vary depending on the

594 specific feldspar and surface temperature environment. For example, Kober et al. (2005)

595 measured cosmogenic ^{21}Ne abundances in sanidine from a welded tuff in the Atacama Desert

596 that were indistinguishable from what would be expected given theoretical ^{21}Ne production rates

597 for sanidine and the known exposure duration, suggesting that no diffusive loss of cosmogenic

598 ^{21}Ne occurred. Complete cosmogenic ^{21}Ne retention suggests that the sanidine studied by Kober

599 et al. (2005) is significantly more retentive to neon than the two sanidine samples we conducted

600 stepwise degassing experiments on here, especially given the high amplitude temperature

601 variations and peak temperatures that rocks experience in extreme environments like the

602 Atacama Desert (McKay et al., 2003; McFadden et al., 2005). Similarly, the lunar surface

603 experiences extreme variations in temperature during a lunar day cycle, with peak temperatures

604 in excess of 100 °C and temperature minima less than −150 °C (Keihm and Langseth, 1973).

605 However, because lunar 76535 anorthite is so retentive, Tremblay and Shuster (2016) were able

606 to measure cosmogenic neon abundances in multiple anorthite grains and calculate an accurate

607 estimate of the effective lunar surface temperature (75.5 ± 4.2 °C) over the 142 Ma exposure

608 history of sample 76535. For any of the diffusion parameters we obtained for the other feldspars,

609 we would predict substantially lower and incorrect effect lunar surface temperatures.

610

611 **5. Conclusions**

612 We present stepwise neon degassing experiments on feldspars of various compositions and

613 geologic origins. This suite of experiments reveals that neon diffusion behavior and kinetics vary

614 significantly amongst different feldspars. Comparison with argon stepwise degassing

615 experiments on the same feldspars provides insight into the source of complex noble gas

616 diffusion behavior. For some feldspars, the absence of nonlinear Arrhenius behavior in neon

617 experiments conducted at lower temperatures suggests that the nonlinear behavior observed in

618 argon experiments resulted from temperature-dependent structural transformations. For other

619 feldspars, nonlinear Arrhenius behavior observed in both neon and argon experiments suggests

620 that some sample-specific material property is contributing to complex diffusion behavior. When

621 extrapolated down to planetary surface temperatures, the set of available neon diffusion kinetics

622 predicts a wide range of temperatures and exposure durations over which cosmogenic noble gas

623 paleothermometry may be applicable. This wide range indicates that (1) sample specific

624 diffusion kinetics will be necessary for quantitative applications, and (2) the temperature

625 sensitivity of cosmogenic noble gas paleothermometry will depend greatly on a combination of

626 the specific feldspar and surface thermal environment of interest.

References Cited

636   Bachmann O., Dungan M. A. and Lipman P. W. (2002) The Fish Canyon Magma Body, San
637   Juan Volcanic Field, Colorado: Rejuvenation and Eruption of an Upper-Crustal Batholith. *J.*
638   *Petrol.* **43**, 1469–1503.

639   Balco G. and Shuster D. L. (2009) Production rate of cosmogenic ^{21}Ne in quartz estimated from
640   ^{10}Be, ^{26}Al, and ^{21}Ne concentrations in slowly eroding Antarctic bedrock surfaces. *Earth*
641   *Planet. Sci. Lett.* **281**, 48–58.

642   Berger G. W. and York D. (1981) Geothermometry from ^{40}Ar/^{39}Ar dating experiments.
643   *Geochim. Cosmochim. Acta* **45**, 795–811.

644   Brown W. L., Openshaw R. E., McMillan P. F. and Henderson M. B. (1984) A review of the
645   expansion behavior of alkali feldspars: coupled variations in cell parameters and possible
646   phase transitions. *American Mineralogist* **69**, 1058–1071.

647   Cassata W. S. and Renne P. R. (2013) Systematic variations of argon diffusion in feldspars and
648   implications for thermochronometry. *Geochim. Cosmochim. Acta* **112**, 251–287.

649   Cassata W. S., Shuster D. L., Renne P. R. and Weiss B. P. (2010) Evidence for shock heating
650   and constraints on Martian surface temperatures revealed by ^{40}Ar/^{39}Ar thermochronometry
651   of Martian meteorites. *Geochim. Cosmochim. Acta* **74**, 6900–6920.

652   Crank J. (1975) *The Mathematics of Diffusion*., Oxford University Press, London.

653   Evernden J. F., Curtis G. H., Kistler R. W. and Obradovich J. D. (1960) Argon diffusion in
654   glauconite, microcline, sanidine, leucite and phlogopite. *Am. J. Sci.* **258**, 583–604.

655   Fechtig H., Gentner W. and Zähringer J. (1960) Argonbestimmungen an Kaliummineralien—VII
656   Diffusionsverluste von Argon in Mineralien und ihre Auswirkung auf die Kalium-Argon-
657   Altersbestimmung. *Geochim. Cosmochim. Acta* **19**, 70–79.

658   Fechtig H. and Kalbitzer S. (1966) The Diffusion of Argon in Potassium-Bearing Solids. In
659   *Potassium Argon Dating* pp. 68–107.

660   Foit F. F. Jr. and Peacor D. R. (1973) The Anorthite Crystal Structure at 410 and 830 °C.
661   *American Mineralogist* **58**, 665–675.

662   Foland K. A. and Xu Y. (1990) Diffusion of ^{40}Ar and ^{39}Ar in irradiated orthoclase. *Geochim.*
663   *Cosmochim. Acta* **54**, 3147–3158.

664   Garrick-Bethell, I., Weiss, B.P., Shuster, D.L., Tikoo, S.M., Tremblay, M.M., 2017. Further
665   evidence for early lunar magnetism from troctolite 76535. Journal of Geophysical Research:
666   Planets.

667   Gautheron C. and Tassan-Got L. (2010) A Monte Carlo approach to diffusion applied to noble
668   gas/helium thermochronology. *Chem. Geol.* **273**, 212–224.

669   Gerling E. K., Levski L. K. and Morozova I. M. (1963) On the diffusion of radiogenic argon
670   from minerals. *Geokhimiya* **Vol: No. 6**. Available at:
671   http://www.osti.gov/scitech/biblio/4712579.

672   Gourbet L., Shuster D. L., Balco G., Cassata W. S., Renne P. R. and Rood D. (2012) Neon
673   diffusion kinetics in olivine, pyroxene and feldspar: Retentivity of cosmogenic and
674   nucleogenic neon. *Geochim. Cosmochim. Acta* **86**, 21–36.

675   Harrison T. M., Lovera O. M. and Matthew T. H. (1991) ^{40}Ar/^{39}Ar results for alkali feldspars
676   containing diffusion domains with differing activation energy. *Geochim. Cosmochim. Acta*
677   **55**, 1435–1448.

678   Harrison T. M. and McDougall I. (1982) The thermal significance of potassium feldspar K-Ar
679   ages inferred from ^{40}Ar/^{39}Ar age spectrum results. *Geochim. Cosmochim. Acta* **46**, 1811–
680   1820.

681   Herman F., Seward D., Valla P. G., Carter A., Kohn B., Willett S. D. and Ehlers T. A. (2013)
682   Worldwide acceleration of mountain erosion under a cooling climate. *Nature* **504**, 423–426.

683   Hodges K. V., Ruhl K. W., Wobus C. W. and Pringle M. S. (2005) ^{40}Ar/^{39}Ar Thermochronology
684   of Detrital Minerals. *Rev. Mineral. Geochem.* **58**, 239–257.

685   Hovis G. L., Brennan S., Keohane M. and Crelling J. (1999) High-Temperature X-ray
686   investigation of sanidine - analbite crystalline solutions: thermal expansion, phase
687   transitions, and volumes of mixing. *The Canadian Mineralogist* **37**, 701–709.

688   Hovis G. L., Medford A., Conlon M., Tether A. and Romanoski A. (2010) Principles of thermal
689   expansion in the feldspar system. *Am. Mineral.* **95**, 1060–1068.

690   Huber C., Cassata W. S. and Renne P. R. (2011) A lattice Boltzmann model for noble gas
691   diffusion in solids: The importance of domain shape and diffusive anisotropy and
692   implications for thermochronometry. *Geochim. Cosmochim. Acta* **75**, 2170–2186.

Jourdan F., Moynier F., Koeberl C. and Eroglu S. (2011) ^{40}Ar/^{39}Ar age of the Lonar crater and consequence for the geochronology of planetary impacts. *Geology* **39**, 671–674.

Keihm S. J. and Langseth M. G. Jr (1973) Surface brightness temperatures at the Apollo 17 heat flow site: Thermal conductivity of the upper 15 cm of regolith. In *Lunar and Planetary Science Conference Proceedings* adsabs.harvard.edu. p. 2503.

Ketcham R. A. (2005) Computational methods for quantitative analysis of three-dimensional features in geological specimens. *Geosphere* **1**, 32–41.

Ketcham R. A. and Carlson W. D. (2001) Acquisition, optimization and interpretation of X-ray computed tomographic imagery: applications to the geosciences. *Comput. Geosci.* **27**, 381–400.

Kober F., Ivy-Ochs S., Leya I., Baur H., Magna T., Wieler R. and Kubik P. W. (2005) In situ cosmogenic 10Be and 21Ne in sanidine and in situ cosmogenic 3He in Fe–Ti-oxide minerals. *Earth Planet. Sci. Lett.* **236**, 404–418.

Koning A. J., Rochman D., Kopecky J., Ch. Sublet J., Bauge E., Hilaire S., Romain P., Morillon B., Duarte H., van der Marck S., Pomp S., Sjostrand H., Forrest R., Henriksson H., Cabellos O., Goriely S., Leppanen J., Leeb H., Plompen A. and Mills R. (2015) TENDL-2015. *TENDL-2015: TALYS-based evaluated nuclear data library*. Available at: https://tendl.web.psi.ch/tendl_2015/tendl2015.html.

Lovera O. M., Grove M. and Harrison T. M. (2002) Systematic analysis of K-feldspar ^{40}Ar/^{39}Ar step heating results II: relevance of laboratory argon diffusion properties to nature. *Geochim. Cosmochim. Acta* **66**, 1237–1255.

Lovera O. M., Grove M., Harrison T.M., and Mahon K. I. (1997) Systematic analysis of K-feldspar ^{40}Ar/^{39}Ar step heating results: I. Significance of activation energy determinations. *Geochim. Cosmochim. Acta* **61**, 3171–3192.

Lovera O. M., Harrison T. M. and Boehnke P. (2015) Comment on "Systematic variations of argon diffusion in feldspars and implications for thermochronometry" by Cassata and Renne. *Geochim. Cosmochim. Acta* **151**, 168–171.

Lovera O. M., Heizler M. T. and Harrison T.M. (1993) Argon diffusion domains in K-feldspar II: kinetic properties of MH-10. *Contrib. Mineral. Petrol.* **113**, 381–393.

Lovera O. M. and Richter F. M. (1989) The ^{40}Ar/^{39}Ar Thermochronometry for Slowly Cooled Samples. *J. Geophys. Res.* **94**, 17–917.

Lovera O. M., Richter F. M. and Harrison T. M. (1991) Diffusion domains determined by ^{39}Ar released during step heating. *J. Geophys. Res.* **96**, 2057–2069.

McFadden L. D., Eppes M. C., Gillespie A. R. and Hallet B. (2005) Physical weathering in arid landscapes due to diurnal variation in the direction of solar heating. *GSA Bulletin* **117**, 161–173.

729   McKay C. P., Friedmann E. I., Gómez-Silva B., Cáceres-Villanueva L., Andersen D. T. and
730   Landheim R. (2003) Temperature and moisture conditions for life in the extreme arid region
731   of the Atacama desert: four years of observations including the El Niño of 1997-1998.
732   *Astrobiology* **3**, 393–406.

733   McLaren A. C. and Marshall D. B. (1974) Transmission electron microscope study of the
734   domain structures associated with the b-, c-, d-, e- and f-reflections in plagioclase feldspars.
735   *Contrib. Mineral. Petrol.* **44**, 237–249.

736   McLaren S., Dunlap W. J. and Powell R. (2007) Understanding K-feldspar ^{40}Ar/^{39}Ar data:
737   reconciling models, methods and microtextures. *J. Geol. Soc. London* **164**, 941–944.

738   Meesters A. G. C. A. and Dunai T. J. (2002) Solving the production–diffusion equation for finite
739   diffusion domains of various shapes: Part I. Implications for low-temperature (U–Th)/He
740   thermochronology. *Chem. Geol.* **186**, 333–344.

741   Megaw H. D., Kempster C. J. E. and Radoslovich E. W. (1962) The structure of anorthite,
742          $CaAl_2Si_2O_8$ II. Description and discussion. *Acta Crystallogr.* **15**, 1017–1035.

743   Min K., Reiners P. W., Nicolescu S. and Greenwood J. P. (2004) Age and temperature of shock
744   metamorphism of Martian meteorite Los Angeles from (U-Th)/He thermochronometry.
745   *Geology* **32**, 677.

746   Parsons I. (2010) Feldspars defined and described: a pair of posters published by the
747   Mineralogical Society. Sources and supporting information. *Mineral. Mag.* **74**, 529–551.

748   Parsons I., Brown W. L. and Smith J. V. (1999) ^{40}Ar/^{39}Ar thermochronology using alkali
749   feldspars: real thermal history or mathematical mirage of microtexture? *Contrib. Mineral.*
750   *Petrol.* **136**, 92–110.

751   Rainey C. S. and Wenk H.-R. (1978) lntensity differences of subsidiary reflections in calcic
752   plagioclase. *American Mineralogist* **63**, 124–131.

753   Reynolds J. H. (1957) Comparative study of argon content and argon diffusion in mica and
754   feldspar. *Geochim. Cosmochim. Acta* **12**, 177–184.

755   Richter F. M., Lovera O. M., Harrison T. M. and Copeland P. (1991) Tibetan tectonics from
756   ^{40}Ar/^{39}Ar analysis of a single K-feldspar sample. *Earth Planet. Sci. Lett.* **105**, 266–278.

757   Schairer J. F. (1950) The Alkali-Feldspar Join in the System $NaAlSiO_4$-$KAlSiO_4$-SiO_2. *J. Geol.*
758   **58**, 512–517.

759   Shuster D. L., Balco G., Cassata W. S., Fernandes V. A., Garrick-Bethell I. and Weiss B. P.
760   (2010) A record of impacts preserved in the lunar regolith. *Earth Planet. Sci. Lett.* **290**,
761   155–165.

762   Shuster D. L. and Cassata W. S. (2015) Paleotemperatures at the lunar surfaces from open
763   system behavior of cosmogenic ^{38}Ar and radiogenic ^{40}Ar. *Geochim. Cosmochim. Acta* **155**,

764   154–171.

765 Shuster D. L. and Farley K. A. (2005a) ^{4}He/^{3}He Thermochronometry: Theory, Practice, and
766   Potential Complications. *Rev. Mineral. Geochem.* **58**, 181–203.

767 Shuster D. L. and Farley K. A. (2005b) Diffusion kinetics of proton-induced ^{21}Ne, ^{3}He, and ^{4}He
768   in quartz. *Geochim. Cosmochim. Acta* **69**, 2349–2359.

769 Shuster D. L. and Farley K. A. (2009) The influence of artificial radiation damage and thermal
770   annealing on helium diffusion kinetics in apatite. *Geochim. Cosmochim. Acta* **73**, 183–196.

771 Shuster D. L., Farley K. A., Sisterson J. M. and Burnett D. S. (2004) Quantifying the diffusion
772   kinetics and spatial distributions of radiogenic ^{4}He in minerals containing proton-induced
773   ^{3}He. *Earth Planet. Sci. Lett.* **217**, 19–32.

774 Smith J. V. and Ribbe P. H. (1969) Atomic movements in plagioclase feldspars: Kinetic
775   interpretation. *Contrib. Mineral. Petrol.* **21**, 157–202.

776 Tremblay M. M., Shuster D. L. and Balco G. (2014a) Cosmogenic noble gas paleothermometry.
777   *Earth Planet. Sci. Lett.* **400**, 195–205.

778 Tremblay M. M., Shuster D. L. and Balco G. (2014b) Diffusion kinetics of ^{3}He and ^{21}Ne in
779   quartz and implications for cosmogenic noble gas paleothermometry. *Geochim.*
780   *Cosmochim. Acta* **142**, 186–204.

781 Tribaudino M., Angel R. J., Cámara F., Nestola F., Pasqual D. and Margiolaki I. (2010) Thermal
782   expansion of plagioclase feldspars. *Contrib. Mineral. Petrol.* **160**, 899–908.

783 Turner G. (1971) ^{40}Ar-^{39}Ar ages from the lunar maria. *Earth Planet. Sci. Lett.* **11**, 169–191.

784 Van Tendeloo G., Ghose S. and Amelinckx S. (1989) A dynamical model for the P1—I1 phase
785   transition in anorthite, $CaAl_2Si_2O_8$. *Phys. Chem. Miner.* **16**, 311–319.

786 Villa I. M. (2006) From nanometer to megameter: Isotopes, atomic-scale processes, and
787   continent-scale tectonic models. *Lithos* **87**, 155–173.

788 Villa I. M. and Hanchar J. M. (2013) K-feldspar hygrochronology. *Geochim. Cosmochim. Acta*
789   **101**, 24–33.

790 Wolf R. A., Farley K. A. and Kass D. M. (1998) Modeling of the temperature sensitivity of the
791   apatite (U–Th)/He thermochronometer. *Chem. Geol.* **148**, 105–114.

792 Ziegler J. F., Ziegler M. D. and Biersack J. P. (2010/6) SRIM – The stopping and range of ions
793   in matter (2010). *Nucl. Instrum. Methods Phys. Res. B* **268**, 1818–1823.

Tables

Table 1. Description of feldspar samples studied in diffusion experiments.

Sample	Description	Phase	An	Ab	Or
			Composition		
BMk	Granitic pegmatite, Benson Mines, NY USA	Orthoclase	0.0	3.0	97.0
FCs	Rhyolitic ignimbrite, Fish Canyon Tuff, CO USA	Sanidine	1.0	27.0	72.0
GSs	Rhyolitic ash, Gulf of Salerno, Italy	Sanidine	3.7	30.5	65.8
SURTp	Basaltic lava, Surtsey, Iceland	Labradorite	59.6	39.6	0.8
OREGp	Basaltic lava, Plush, OR USA	Labradorite	63.9	35.4	0.7
GV-09	Anorthosite, Grass Valley, CA USA	Anorthite	94.2	5.2	0.6
76535	Troctolite, Moon	Anorthite	96.2	3.5	0.3

Table 2. Summary of neon diffusion parameters. 1σ uncertainties are reported.

Sample	Spherical equiv. radius (μm)[a]	E_a (kJ/mol)	±	$\ln(D_0/a^2)$	±	Apparent D_0 (cm^2/s)[b]
BMk-D	283, 271	91.7	2.1	4.32	0.44	5.52E-02
FCs-A	308, 276	83.6	1.8	1.14	0.34	2.38E-03
FCs-C	327, 328	86.3	1.4	1.90	0.24	7.19E-03
GSs-A	178, 205	83.3	1.5	3.88	0.32	2.04E-02
SURTp-B	307	94.3	1.2	4.72	0.24	1.06E-01
OREGp-A	320, 336	102.1	1.9	6.28	0.46	6.03E-01
GV-09-A	230	103.3	3.5	12.84	0.89	1.99E+02
76535-B[c]	296, 244	110.7	1.6	0.73	0.32	8.86E-01

[a]Spherically equivalent radii were calculated in several different ways. In the first instance, the radius was calculated from the surface area to volume ratio (SA/V) of the crystal analzyed using optical microscope measurements. For some of the ^{21}Ne stepwise degassing experiments, a second radius is listed that was calculated from the SA/V determined from X-ray computed tomography measurements (Table S2).
[b]Calculated assuming the spherically equivalent radius of the crystals analyzed defines *a*, the diffusive lengthscale.
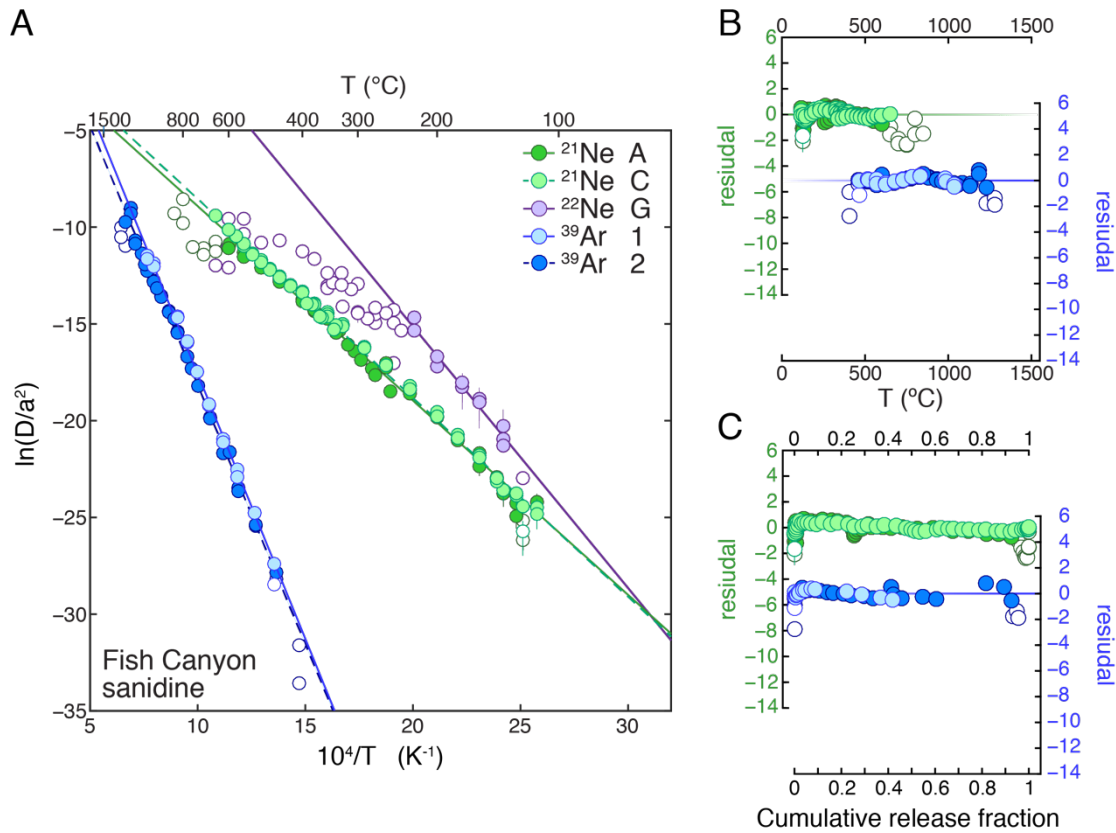[c]Stepwise degassing experiment data presented in Tremblay and Shuster (2016).

800 **Table 3.** Best fit multiple diffusion domain model parameters.

| Sample	Domain	E_a (kJ/mol)	$\ln(D_0/a^2)$	f	Misfit
BMk-D	1	91.5	4.0	0.45	0.17
	2		5.6	0.30	
	3		1.2	0.25	
OREGp-A	1	96.9	2.4	0.74	0.16
	2		7.4	0.26	
GV-09-A	1	108.4	14.9	0.76	0.33
	2		19.2	0.08	
	3		8.0	0.08	
	4		4.3	0.08	

801

802

Figures
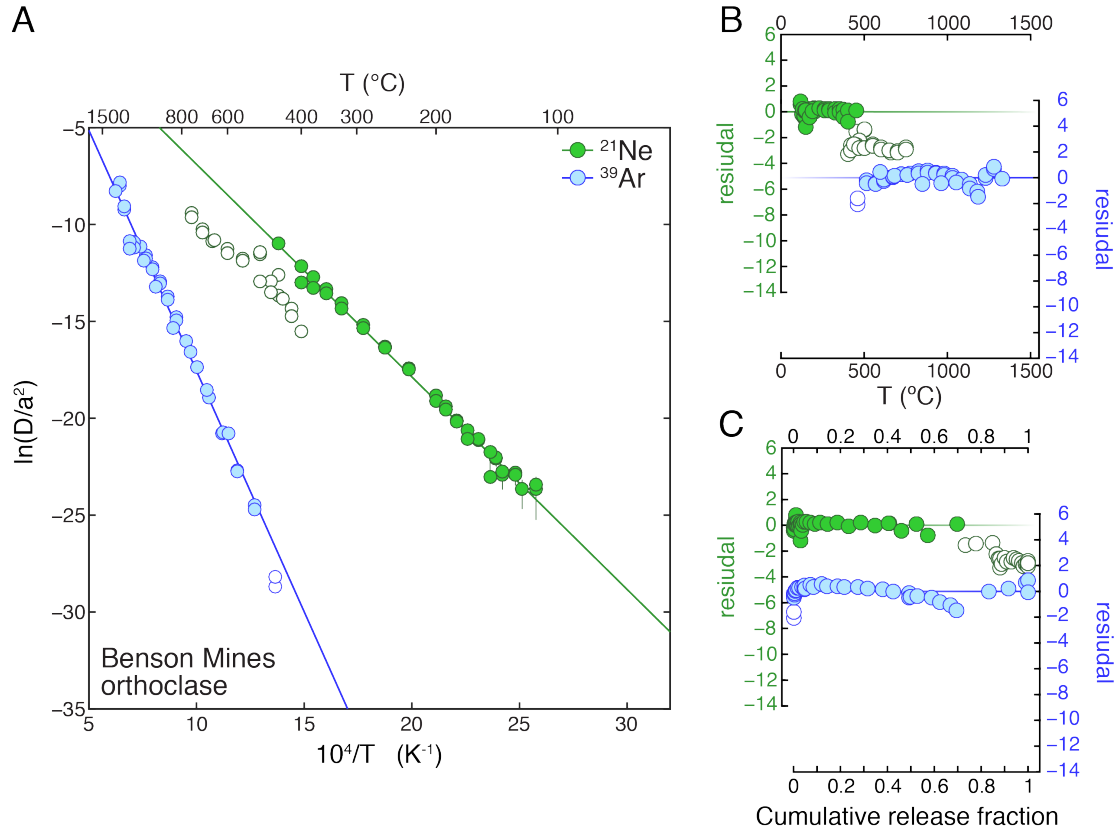

804

Fig. 1. Arrhenius plot (A) and residual plots (B-C) for diffusion of proton-induced [21]Ne (green),

neutron-induced [39]Ar (blue; data from Cassata and Renne, 2013), and neutron-induced [22]Ne

(purple; data from Gourbet et al., 2012) in different crystals of Fish Canyon sanidine. For visual

clarity, residuals are not shown for neutron-induced [22]Ne. D/a^2 values are normalized to s^{-1}.

Uncertainties in $\ln(D/a^2)$ estimated using a Monte Carlo approach (Tremblay et al., 2014b) are

shown, although in most cases the uncertainty is smaller than the symbol plotted. Linear

regressions in (A) are fit through the filled symbols and used to determine E_a and $\ln(D_0/a^2)$,

assuming an Arrhenian dependence of diffusivity on temperature (Eq. 1). Residuals, defined as

the difference between the calculated $\ln(D/a^2)$ from a given heating step and the expected

$\ln(D/a^2)$ from the linear regression at the same temperature, are plotted against temperature (B)

and cumulative gas release fraction (C). Filled symbols are the same as in (A).

816
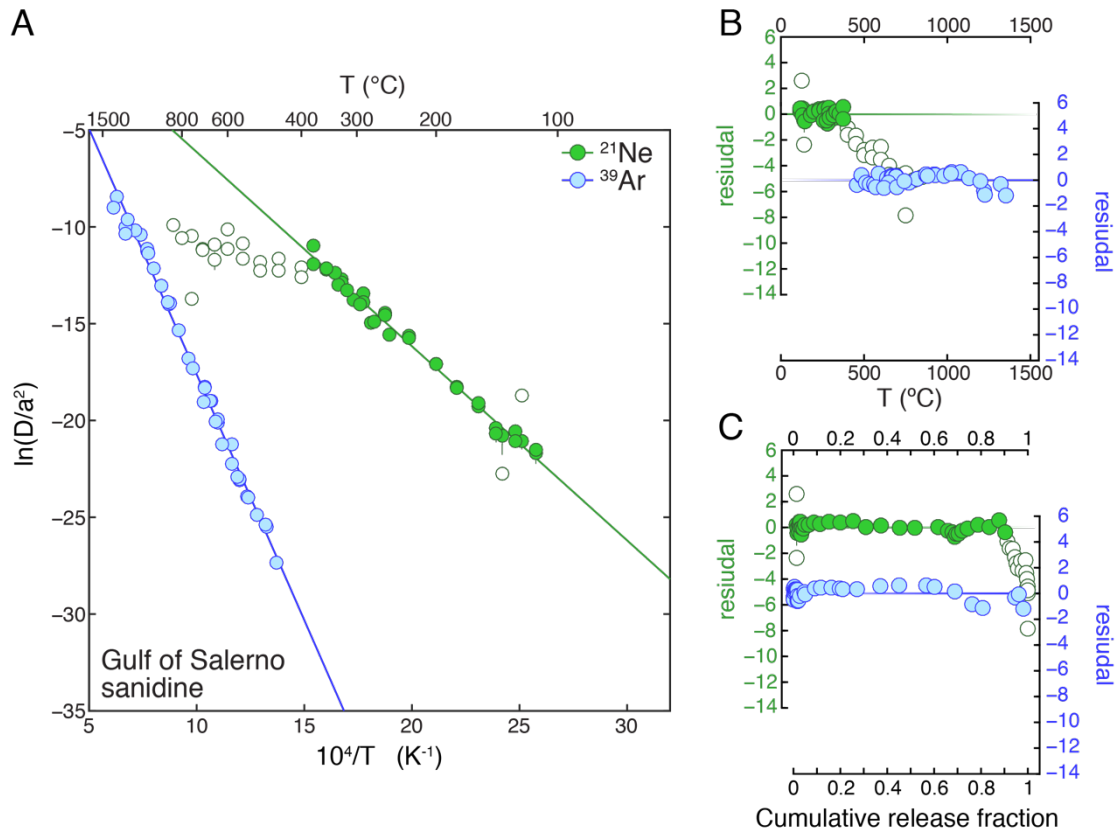
817

818 **Fig. 2.** Arrhenius plot (A) and residual plots (B-C) for diffusion of proton-induced [21]Ne (green)

819 and neutron-induced [39]Ar (blue; data from Cassata and Renne, 2013) in different crystals of Gulf

820 of Salerno sanidine. Units, uncertainties, linear regressions, and residuals are as described for
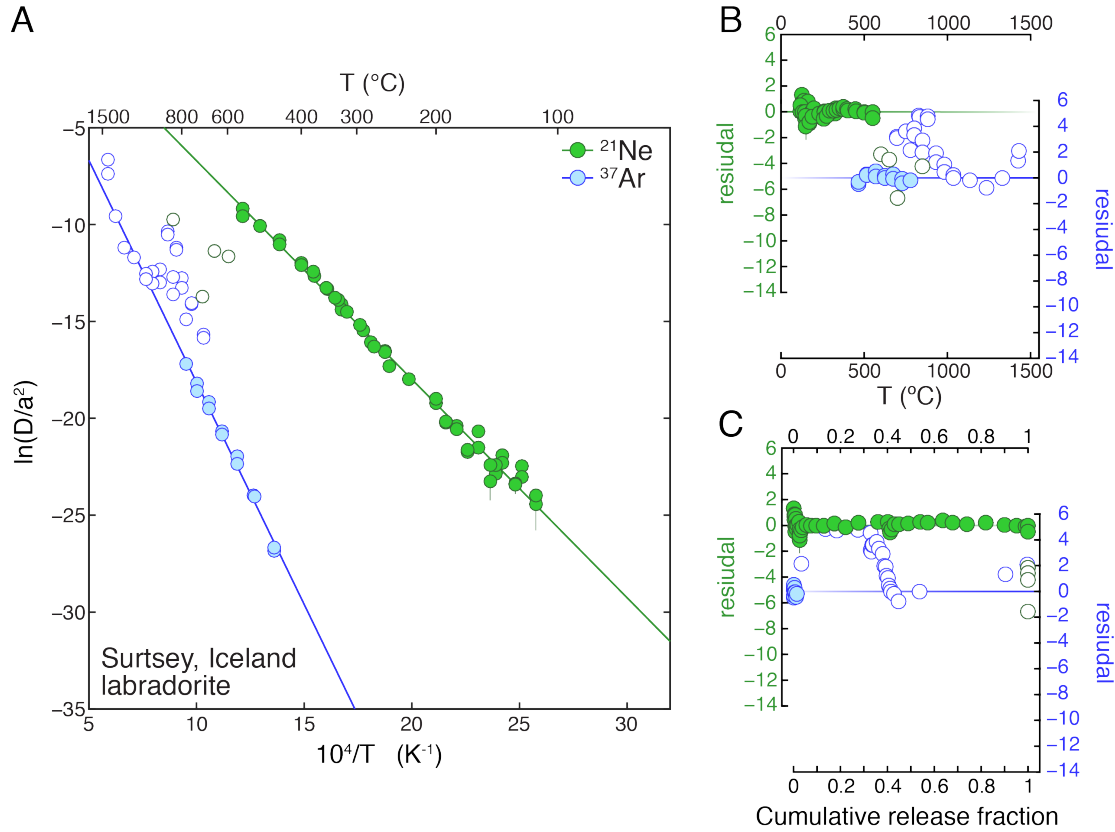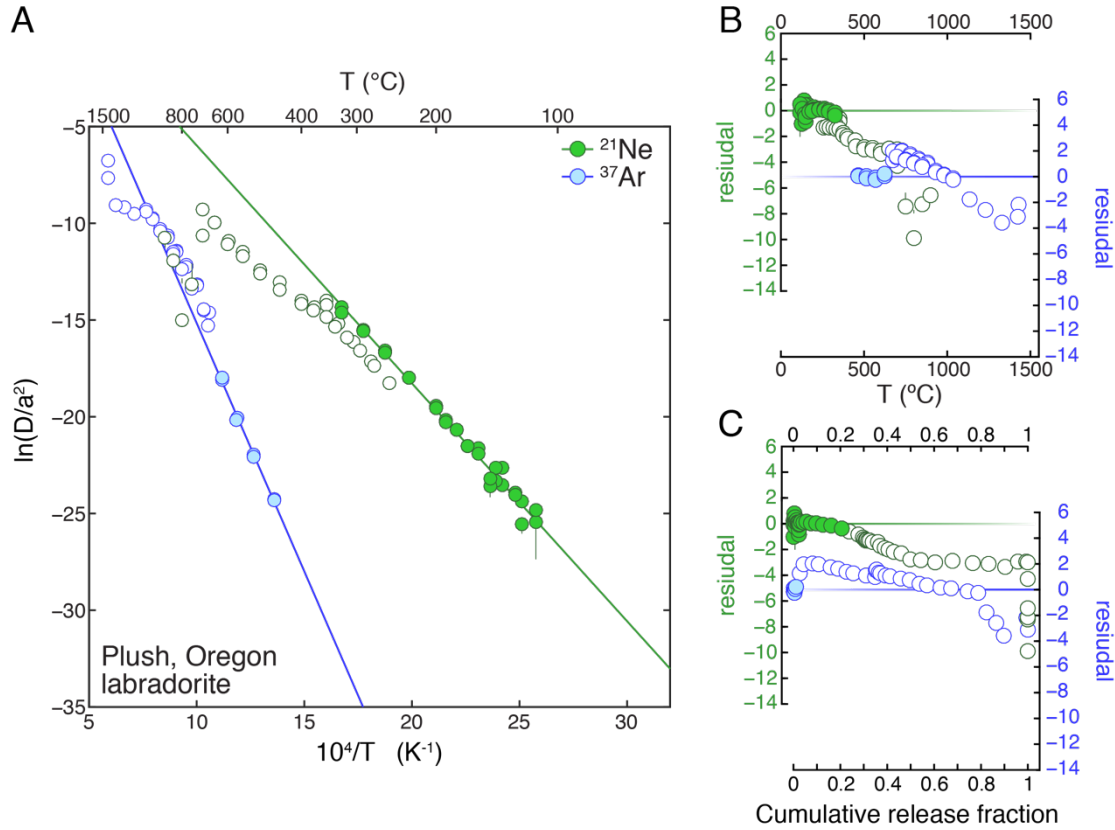
821 Fig. 1.
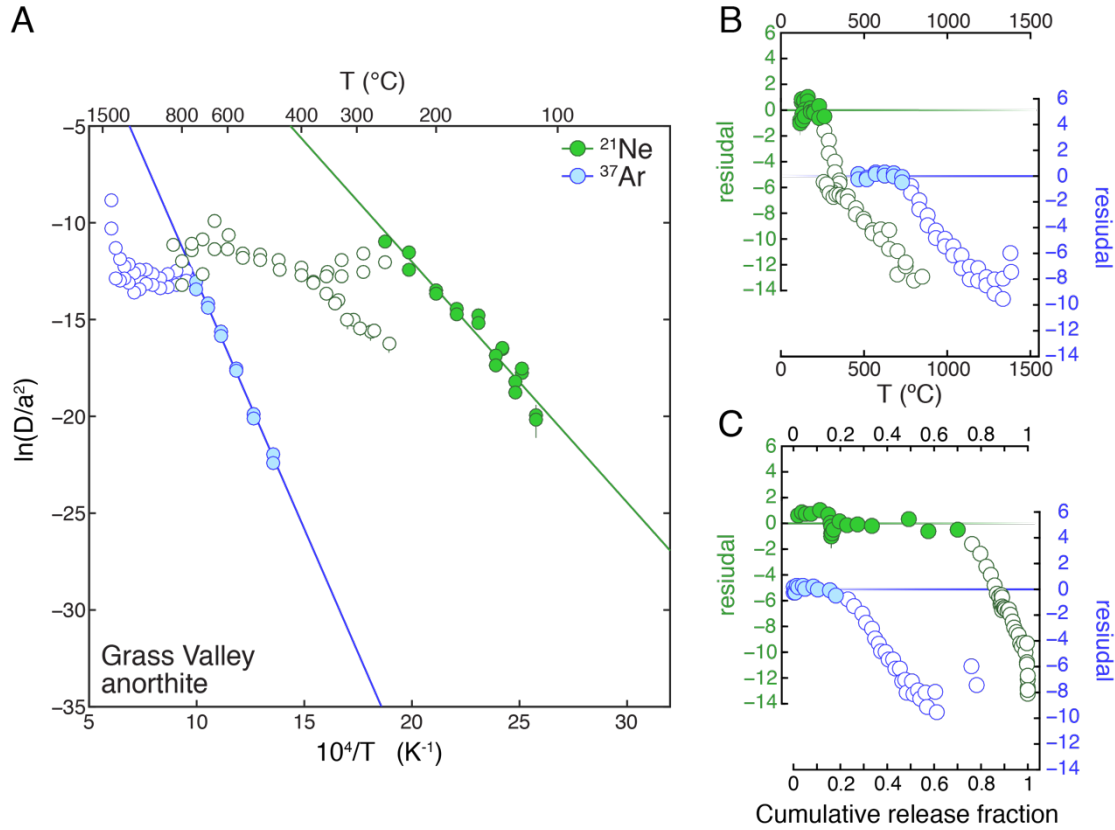
822

Fig. 3. Arrhenius plot (A) and residual plots (B-C) for diffusion of proton-induced [21]Ne (green) and neutron-induced [39]Ar (blue; data from Cassata and Renne, 2013) in different crystals of Benson Mines orthoclase. Units, uncertainties, linear regressions, and residuals are as described for Fig. 1.

828

Fig. 4. Arrhenius plot (A) and residual plots (B-C) for diffusion of proton-induced ²¹Ne (green)

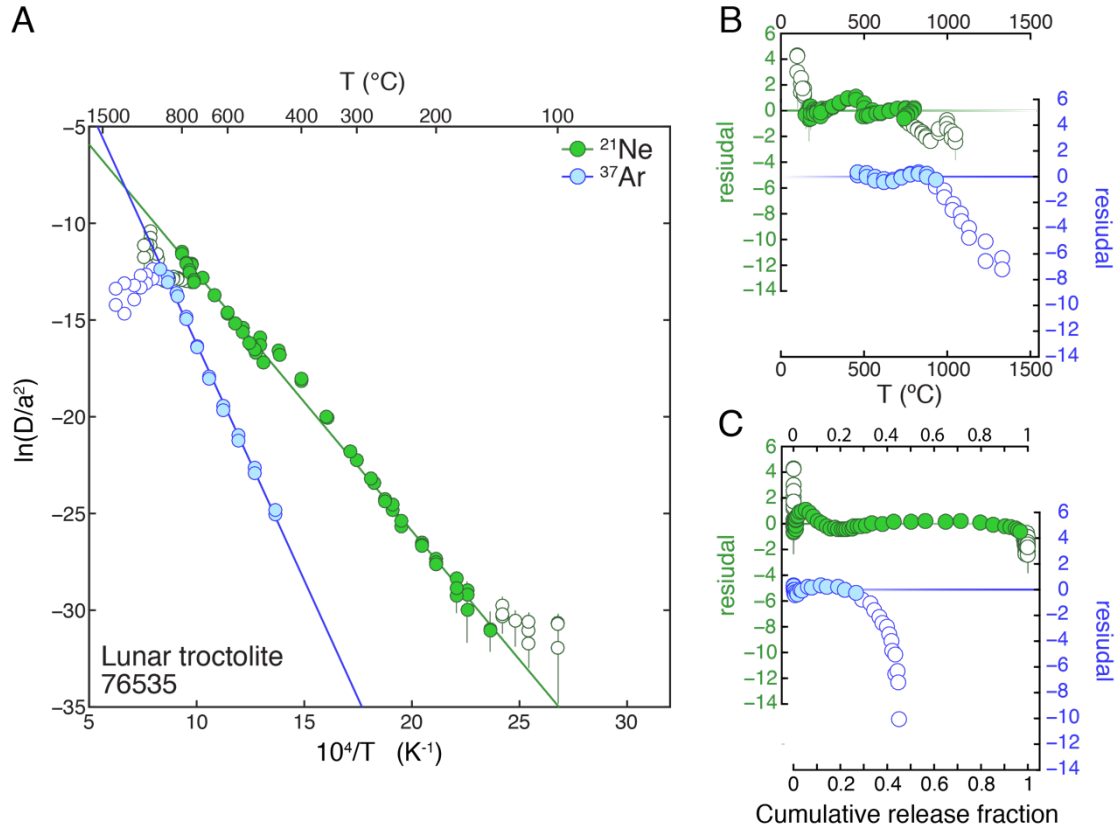and neutron-induced ³⁷Ar (blue; data from Cassata and Renne, 2013) in different crystals of

Surtsey, Iceland labradorite. Units, uncertainties, linear regressions, and residuals are as

described for Fig. 1.

833

Fig. 5. Arrhenius plot (A) and residual plots (B-C) for diffusion of proton-induced ^{21}Ne (green) and neutron-induced ^{37}Ar (blue; data from Cassata and Renne, 2013) in different crystals of Plush, Oregon labradorite. Units, uncertainties, linear regressions, and residuals are as described for Fig. 1.

**Fig. 6.** Arrhenius plot (A) and residual plots (B-C) for diffusion of proton-induced ^{21}Ne (green) and neutron-induced ^{37}Ar (blue; data from Cassata and Renne, 2013) in different crystals of Grass Valley anorthite. Units, uncertainties, linear regressions, and residuals are as described for Fig. 1.

**Fig. 7.** Arrhenius plot (A) and residual plots (B-C) for diffusion of neutron-induced [21]Ne (green; data from Garrick-Bethell et al., 2017) and [39]Ar (blue; data from Cassata and Renne, 2013) in different crystals of lunar 76535 anorthite. Units, uncertainties, linear regressions, and residuals are as described for Fig. 1.

848
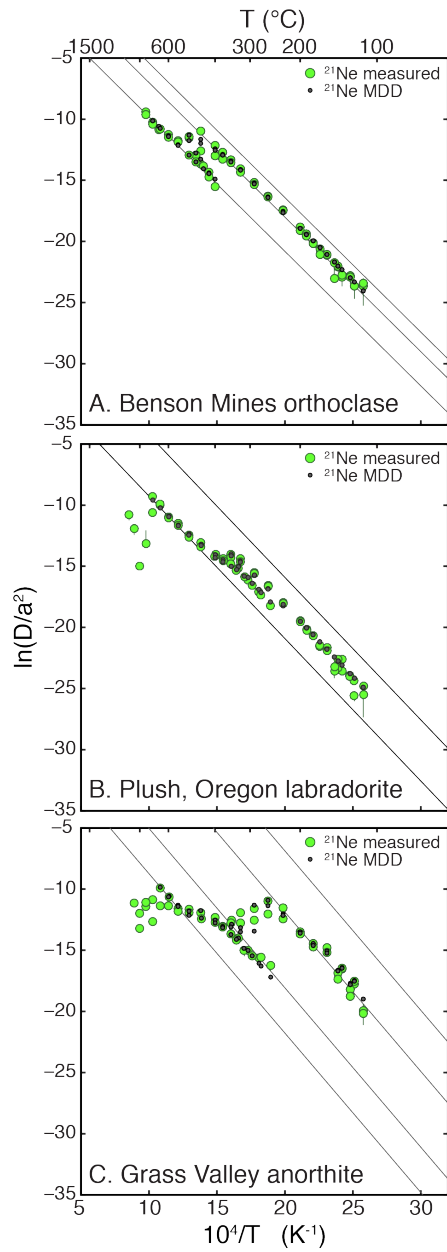
Fig. 8. Arrhenius plots comparing calculated diffusivities from multiple diffusion domain

(MDD) models (black) to calculated diffusivities from neon stepwise degassing experiments

(green) for Benson Mines orthoclase (A), Plush labradorite (B), and Grass Valley anorthite (C).

Lines correspond to diffusion parameters characterizing each diffusion domain, which are listed

in Table 3 along with the fraction of gas comprising each domain and the misfit statistic of the

models shown.
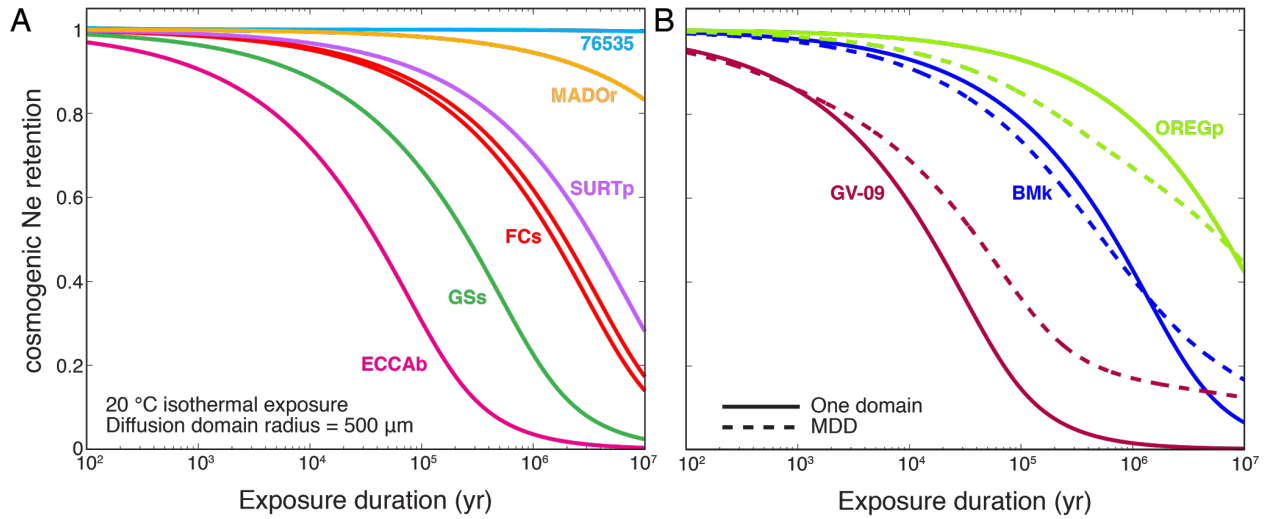
Fig. 9. Demonstration of the variability of neon retentivity in feldspars. Using the neon diffusion parameters reported here and elsewhere (Gourbet et al., 2012; Garrick-Bethell et al., 2017), we calculate how neon retention evolves as a function of exposure duration assuming a constant exposure temperature of 20 °C after Wolf et al. (1998). In (A), we show neon retention curves for the six feldspars that exhibit relatively simple linear Arrhenius behavior. Simple linear Arrhenius behavior suggests that the physical grain size defines the diffusion lengthscale for these feldspars; therefore we normalized the diffusion lengthscale to a common spherically equivalent radius of 500 μm. In (B), we show neon retention curves for exhibiting complex Arrhenius behavior using diffusion parameters calculated both from the initial linear Arrhenius array (solid curves) observed in stepwise degassing experiments as well as using an MDD model (dashed curves). As discussed in the text, we use the grain size analyzed in the stepwise degassing experiment for these calculations, as there is no straightforward way to normalize the diffusion lengthscale for feldspars exhibiting complex diffusion behavior.